Characterization of kaolinized nontronite by visible to near infrared (VNIR) reflectance spectroscopy: implication for the genesis of compositional stratigraphy on Mars

Xiaorong Qin[1,2,3], Jiacheng Liu[4], Wei Tan[1,2]*, Hongping He[1,2,3], Joseph Michalski[4], Yu Sun[5], Shangying Li[6], Binlong Ye[4], Yiliang Li[4]

1 CAS Key Laboratory of Mineralogy and Metallogeny/Guangdong Provincial Key Laboratory of Mineral Physics and Materials, Guangzhou Institute of Geochemistry, Chinese Academy of Sciences, Guangzhou, China

2 CAS Center for Excellence in Deep Earth Science, Guangzhou, China

3 University of Chinese Academy of Sciences, Beijing, China

4 Laboratory for Space Research, University of Hong Kong, Hong Kong, China

5 Key Laboratory of Earth and Planetary Physics, Institute of Geology and Geophysics, Chinese Academy of Sciences (CAS), Beijing, China

6 School of Land Engineering, Chang'an University, Xi'an, China

* Corresponding author: Wei Tan (tanwei@gig.ac.cn)

Key points:

- VNIR reflectance spectroscopy is effective in assessing the OH and H_2O content in different stages of kaolinized nontronite.
- The VNIR data set is reliable for identifying kaolinite/ nontronite ratios and weathering intensities in a basaltic weathering succession.
- The continuous variation of BD1400/BD1900 ratios suggest the compositional stratigraphy on Mars was formed by a chemical weathering process.

Abstract

Compositional stratigraphy, consisting of Al-rich kaolinite overlying Fe/Mg-richnontronite, is sporadically distributed within 40°S to 30°N on Mars. The compositional stratigraphy was considered a typical product of a warm and wet climate, and a window into understanding the atmospheric conditions of early Mars. However, the question remains as to whether the compositional stratigraphy was formed by chemical weathering or sedimentation. Variations in mineralogical/ geochemical properties along the compositional stratigraphy can provide important clues for interpreting the genesis of the compositional stratigraphy. Visible to near infrared (VNIR) reflectance spectroscopy has been used as an effective tool to quantitatively characterize the abundance of kaolinite, nontronite, and weathering intensity in a basaltic weathering succession, as demonstrated by a terrestrial regolith profile. Nevertheless, the VNIR spectra could be influenced by primary minerals and organics in a basalt succession. To test the effectiveness of spectral parameters, the stepwise transformation of nontronite to kaolinite was experimentally modeled and quantitatively investigated using thermogravimetric (TG) and VNIR. The correlation between BD1400 and the content of OH, BD1900 and the H_2O content, and BD1400/BD1900 and the OH/H_2O ratio were quantitatively constrained to demonstrate their effectiveness as spectral proxies. The obtained data set was also compared with the VNIR spectra from the compositional stratigraphy on Mars, and the continuous variations of the spectral proxies suggest the compositional stratigraphy is formed by a

surface chemical weathering process. Accordingly, Mars likely had a warm and wet climate that could maintain liquid water on its surface over a geologic time span.

Plain Language Summary

Compositional stratigraphy consisting of kaolinite overlying nontronite is an intriguing landscape on the surface of Mars. However, it is still unclear how the compositional stratigraphy is formed. An analogous study suggests that it may have been formed by top-down chemical weathering as is the case with a terrestrial regolith profile, since the features of spectral proxies BD1400/BD1900 in the compositional stratigraphy become progressively stronger from bottom to top. Nevertheless, the aforementioned spectral proxies could potentially be influenced by variations in protolithic minerals and/or organics in the basaltic succession. To test the effectiveness of spectral parameters on weathering intensity in a basaltic succession and to discuss the genesis of compositional stratigraphy, the stepwise transformation of nontronite to kaolinite was experimentally modeled and quantitatively investigated using TG and VNIR. Accordingly, the gradual upward increasing trend of VNIR spectra ratios BD1400/BD1900 in the compositional stratigraphy on the Mars reflect gradual decomposition of nontronite, formation of kaolinite and increasing weathering intensity. Therefore, the compositional stratigraphy on the Mars is likely formed by a surface chemical weathering process and Mars likely experienced a warm and wet climate capable of sustaining liquid water on its surface over a geologic time span.

1 Introduction

Clay minerals have been discovered at numerous sites on the Martian surface, including the Nili Fossae region, north of the Syrtis Major volcanic plateau, in the Mawrth Vallis region, and Gale Crater (Bibring et al., 2006; Bristow et al., 2021; Carter et al., 2013; Ehlmann et al., 2011a, 2011b; Viviano et al., 2013). One of the most exciting discoveries is the compositional stratigraphy ubiquitous in the Eridania Basin, Noachis Terra, Nili Fossae, Valles Marineris and Mawrth Vallis (Figure 1a), located within 40 °S to 30 °N (Bishop et al., 2018; Carter et al., 2015; Gaudin et al., 2011; Michalski et al., 2010, 2013; Wray et al., 2008, 2009). Most of the compositional stratigraphy on the Mars developed from the Late Noachian to the Early Hesperian, and is characterized by Al-rich kaolinite and underlying Fe/Mg nontronite (Figure 1b) (Carter et al., 2015; Gaudin et al., 2011; Liu et al., 2021b; Michalski et al., 2013).

The compositional stratigraphy was considered to be detrital phyllosilicate sediments deposited in lacustrine, alluvial, and aeolian environments due to their layered appearance and served as lithologic evidence for the presence of lakes on the ancient terrains of Mars (Bishop et al., 2020; Lowe et al., 2020; McKeown et al., 2009; Michalski et al., 2010; Michalski & Noe Dobrea, 2007). Nevertheless, the genesis of compositional stratigraphy has also been attributed to top-down chemical weathering of the Fe/Mg-clay bearing crust or to basaltic deposition under different climatic conditions, as the contact between the different Al-rich and Fe/Mg-rich clay units is conformable (Bishop et al., 2018; Carter et al., 2015; Ehlmann et al., 2013; Gainey et al., 2014; Gaudin et al., 2011; Liu et al., 2021b; Ye & Michalski, 2021).

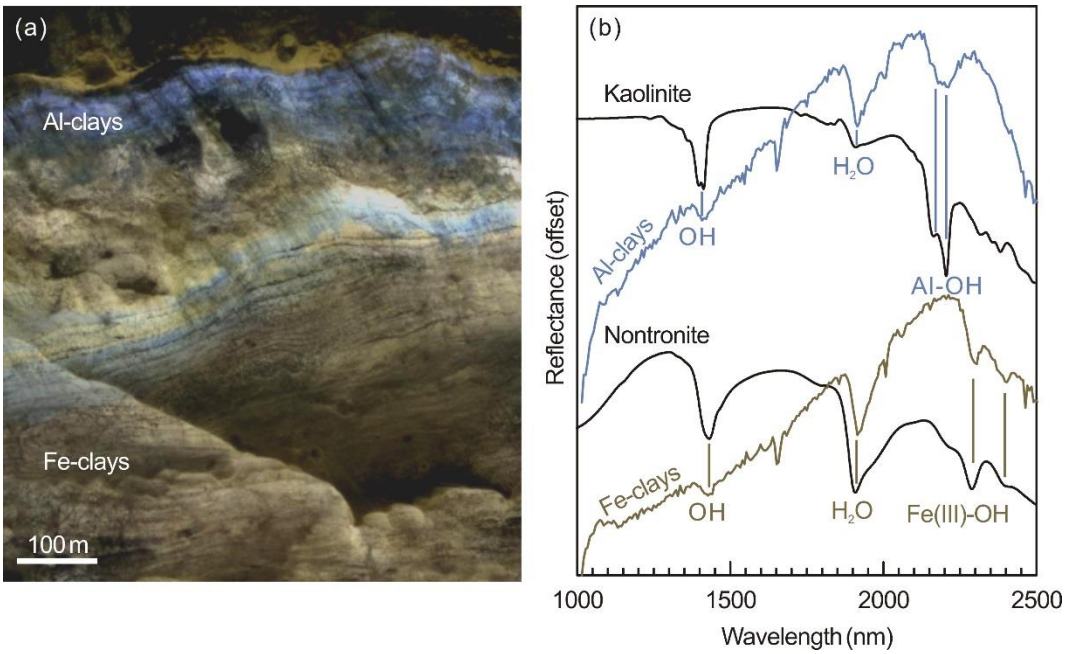

Figure 1. Mineral distribution and infrared spectroscopy of a compositional stratigraphy profile in the Mawrth Vallis region, Mars. (a) View of typically compositional stratigraphy, *i.e.*, Al-clays (blue tone) overlying Fe-clays clays (brown tone), in a Muara crater wall at Mawrth Vallis region (HiRISE image, PSP_004052_2045, located at 340.68° E, 24.35° N, data from Planetary Data System); (b) Comparison between CRISM spectra of Al-clays (blue) and Fe-clays clays (brown) and reference spectra of nontronite and kaolinite. Note that the spectrum of Fe clays is identical to nontronite, and the spectrum of Al-clays is identical to kaolinite. The reference spectra of kaolinite and nontronite were collected from the Maoming Kaolin Clay Company in Guangdong Province, China, and the Uley Graphite Mine in South Australia, respectively.

A proper constraint on the genesis of compositional stratigraphy is a necessary prerequisite for considering it as a window to understanding the past climate and atmospheric conditions of the early Mars (Gaudin et al., 2011; Liu et al., 2021b). Visible/near infrared (VNIR) reflectance spectra provide by far the most reliable and effective data set for identifying chemical and mineralogical features of stratigraphy on the Mars (Chauviré et al., 2021; Cuadros et al., 2016; Fox et al., 2021; Michalski et al., 2015; Pineau et al., 2022; Viviano-Beck et al., 2014). The absorption bands at ~1400, ~1900, ~2200 and ~2290 nm are essentially related to OH (octahedral metal-OH, metal

= Al, Fe and Mg) and H_2O (interlayer water) of kaolinite and nontronite (Bibring et al., 2005; Ehlmann et al., 2013; Pineau et al., 2022). Accordingly, remote sensing VNIR spectra show that the compositional stratigraphy is characterized by Al-rich kaolinite and underlying Fe/Mg-rich nontronite (Figure. 1b) (Carter et al., 2015; Ehlmann et al., 2013; Gaudin et al., 2011; Liu et al., 2021b; Michalski et al., 2013).

Analogous to the compositional stratigraphy on the Mars, some terrestrial basalt weathering successions evolve from nontronite of 2:1 type to kaolinite of 1:1 type due to progressive chemical weathering (Gaudin et al., 2011; Liu et al., 2021a; Prudencio et al., 2002). During the chemical weathering, hydrolysis leads to the formation of OH by the reaction of water with Al and/ or Fe in the octahedral sheet of kaolinite, and leaching tends to reduce both alkaline (earth) elements and H_2O (interlayer water) within the interlayer of nontronite (Cuadros & Michalski, 2013; Liu et al., 2021a). Therefore, the changes in the content of OH and H_2O during the transformation of nontronite to kaolinite are essentially related to the weathering intensity of a basaltic weathering succession (Liu et al., 2021a). It was suggested that the VNIR spectral proxies for variations of OH and H_2O, *e.g.*, BD1400/BD1900, were positively correlated with the weathering intensity of terrestrial weathering successions (Liu et al., 2021a;). The early study also suggested that the compositional stratigraphy in Mawrth Vallis was likely formed by chemical weathering in view of the upward increasing trend of BD1400/BD1900 (Liu et al., 2021b). However, a weathering succession may include sections formed from protoliths with systematic variations in minerals and/or organics, which may affect absorption features at ~1400 and ~1900 nm (Liu et al., 2021a; Tan et

al., 2022). Therefore, whether the band depth of the VNIR absorption and their ratios are due to chemical weathering still remains an open question, and a more reliable and quantitative correlation should be defined to interpret the genesis of compositional stratigraphy on the Mars.

The correlation between VNIR spectral features and weathering intensity of basaltic weathering succession can be quantified using different stages of kaolinized nontronite, whose OH and H_2O variations can be quantitatively analyzed by thermogravimetric analysis (TG). In the present study, the transformation of nontronite to kaolinite was modeled experimentally, avoiding the influences of other minerals and organics in natural samples. The kaolinized nontronite samples with different OH and H_2O contents were characterized using a combination of X-ray diffraction (XRD), scanning electron microscopy (SEM), TG and VNIR. The relationships between OH and BD1400, H_2O content and BD1900, and the suitability of BD1400/BD1900 for characterizing weathering intensity (OH/H_2O) were quantitatively investigated. The obtained dataset allows us to better interpret the near-infrared remote sensing data from Mawrth Vallis on Mars and discuss the genesis of compositional stratigraphy. Our study provides a quantitative correlation between VNIR parameters and weathering intensities of basaltic weathering successions. The obtained results shed light on whether or not compositional stratigraphy is related to top-down chemical weathering, which is critical to understanding the climate and atmospheric conditions of the early Mars.

2 Sample preparation

A series of kaolinized nontronite samples were prepared by converting nontronite to kaolinite with different experimental durations, according to the experiment of Li et al. (2020). The light green colored raw nontronite is from the Uley Graphite Mine in South Australia and is described as N_{Au}, and the chemical formula can be denoted as $M^{+}_{1.05}$ $[Al_{0.26}Fe_{3.71}Mg_{0.03}]$ $[Si_{6.97}Al_{1.03}]$ O_{20} $(OH)_4$ (Ding & Frost, 2002; Frost et al., 2002). In this study, 0.5 g of N_{Au} was added to 20 mL of 0.1 mol L^{-1} $AlCl_3$ solution and transferred to a 250 mL para-phenylene lined autoclave. Given that the duration of these transformations at room temperature may exceed the experimentally observable duration, we performed the transformation experiments at 250 ℃ for 6, 12, 18, 24, 36, 48, 96, and 144 hrs to accelerate the transformation of nontronite to kaolinite (Li et al., 2020). The obtained products were washed with deionized water and centrifuged at 11,000 rpm, and dried at 80 ℃ for 24 hrs, denoted as $N_{Au\text{-}X}$, where X refers to the experimental duration.

3 Analytical Methods

X-ray diffraction (XRD). XRD analysis was performed on a Rigaku MiniFlex-600 X-ray diffractometer with Cu/Kα radiation and a Ni filter operating at a current of 15 mA and voltage of 40 kV. The specimens were scanned from 3° to 70° (2θ) with a step size of 0.02 °and a scanning rate of 10 °/min.

Scanning electron microscopy (SEM). SEM images were obtained using an Analytical Scanning Electron Microscope (TESCAN MIRA 3) equipped with an energy

dispersive X-ray spectrometer (EDS) operated at an accelerating voltage of 20 kV and working distance (WD) of 15-16 mm.

Thermogravimetric analysis (TG). TG analyses were conducted on a Netzsch STA 409PC instrument at the Key Laboratory of Mineralogy and Metallogeny of the Guangzhou Institute of Geochemistry, Chinese Academy of Sciences (GIGCAS). About 10 mg of the samples were heated in a corundum crucible. The samples were heated from 30 to 1000 ℃ at a heating rate of 10 ℃/min in an N_2 atmosphere (60 cm^3 /min). The differential thermogravimetric (DTG) curves were derived from the TG data.

Visible/near infrared (VNIR) reflectance spectroscopy. VNIR reflectance spectroscopy spectra were acquired at wavelengths from 350–2500 nm using an Analytical Spectral Devices (ASD) Terraspec-4 spectrometer at University of Hong Kong (Hong Kong, China), and the spot size is ~20 mm. Reflectance was measured relative to a white reflectance standard Spectral on plate. One hundred scan acquisitions were set to yield an average spectrum for each measurement to improve the signal-to-noise ratio. The ASD spectral files were splice corrected and averaged using the ViewSpecPro (version 6.0) software and then converted to ASCII format. Spectral parameters (e.g., band depth) were calculated according to Liu (2021a, 2021b) and Viviano-Beck (2014).

4 Results

4.1. Phases and morphology of different stages of kaolinized nontronite

Based on the mineral composition and transformation duration of nontronite to kaolinite, the samples can be divided into three stages. The Stage I samples (N_{Au}, $N_{Au\text{-}6h}$ and $N_{Au\text{-}12h}$) were dominated by nontronite, which corresponded to the infantile weathering stage of nontronite. The Stage II samples ($N_{Au\text{-}18h}$, $N_{Au\text{-}24h}$, $N_{Au\text{-}36h}$ and $N_{Au\text{-}48h}$) were composed of nontronite, hematite and kaolinite, corresponding to the intermediate weathering stage of nontronite. The Stage III samples ($N_{Au\text{-}96h}$ and $N_{Au\text{-}144h}$) consisted of kaolinite, hematite, and little nontronite, corresponding to the advanced weathering stage of nontronite.

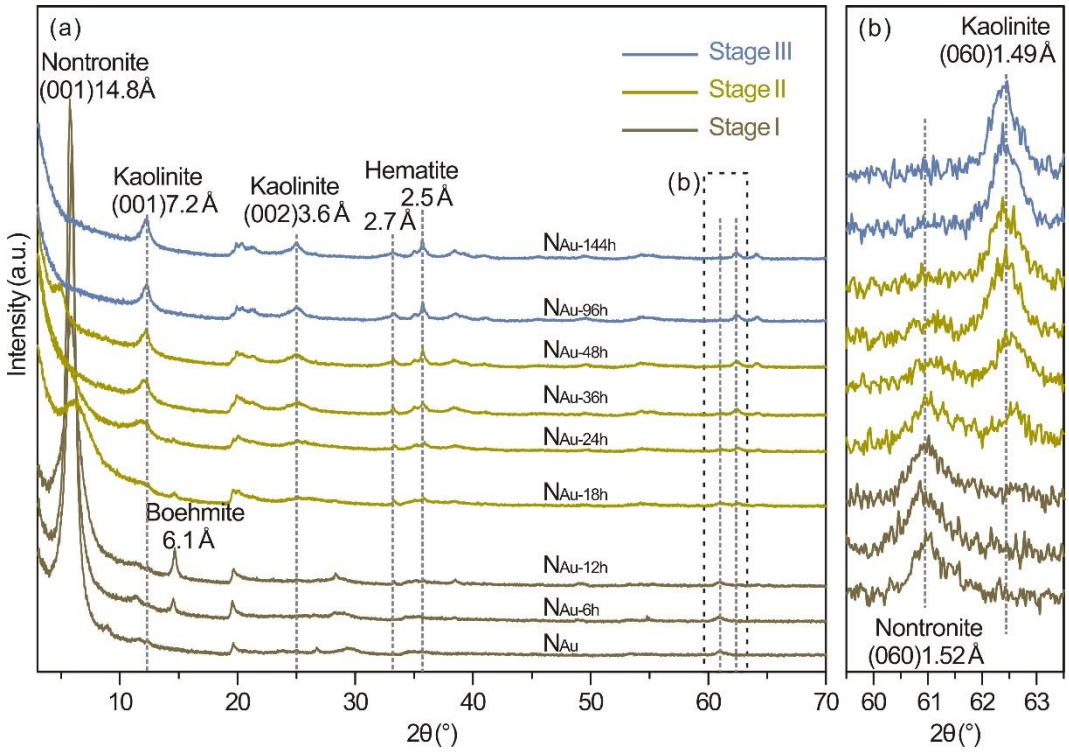

Figure 2. (a) XRD patterns (CuKα) of different stages of kaolinized nontronite; (b) Enlarged XRD patterns of (060) region from the dotted rectangle in (a). Note, the samples are divided into Stage I (N_{Au}, $N_{Au\text{-}6h}$ and $N_{Au\text{-}12h}$), Stage II ($N_{Au\text{-}18h}$, $N_{Au\text{-}24h}$, $N_{Au\text{-}36h}$ and $N_{Au\text{-}48h}$) and Stage III ($N_{Au\text{-}96h}$ and $N_{Au\text{-}144h}$) based on the mineral composition and the duration of experiment.

208 The Stage I samples showed characteristic reflections at ~14.8 and ~1.52 Å (Figure
209 2), corresponding to the (001) and (060) reflections of nontronite (Fernandez-Caliani et
210 al., 2004; Kawi & Yao, 1999). SEM observations showed that the Stage I samples
211 exhibited plate-like morphology with jagged grain boundaries (Figure 3a), which is a
212 typical feature of smectite group minerals (Zhang et al., 2017). The Stage I samples
213 showed gradually weakening reflections of nontronite (*e.g.*, 1.52 Å) with increasing
214 duration of the experiment (Figure 2b), indicating a decrease in nontronite content. In
215 addition, $N_{Au\text{-}6h}$ and $N_{Au\text{-}12h}$ showed characteristic reflections of boehmite at ~6.1 Å
216 (Figure 2a), a common phase precipitated from Al^{3+}-bearing solution (Li et al., 2020).
217 Compared to the Stage I samples, the Stage II samples showed three additional
218 reflections at ~7.2, ~3.6 and ~1.49 Å (Figure 2), corresponding to the (001), (002) and
219 (060) reflections of kaolinite, respectively. Accordingly, the reflections of nontronite
220 gradually decreased at ~14.8 and ~1.52 Å. It is noteworthy that the Stage II samples
221 also displayed two reflections at d-values of ~2.7 and ~2.5 Å (Figure 2a), corresponding
222 to the (104) and (110) reflections of hematite, respectively. Well crystallized kaolinite
223 and hematite were ubiquitous in the Stage II (Figures. 3b-c). As the transformation of
224 nontronite to kaolinite progressed, the reflection intensities of both hematite and
225 kaolinite gradually increased (Figure 2), indicating an increase in their abundance.
226 Moreover, the grain size of kaolinite in the Stage II samples gradually increased from
227 ~2 μm ($N_{Au\text{-}24h}$) to ~6 μm ($N_{Au\text{-}48h}$) (Figures. 3b-c).
228 Compared to the Stage II samples, the Stage III samples showed prominent
229 reflections of kaolinite at ~7.2, ~3.6 and ~1.49 Å, and hematite at ~2.7 and ~2.5 Å, and

these reflections were sharper compared to the Stage II samples (Figure 2). In contrast, the reflections of nontronite were negligible (Figure 2), indicating that the Stage III samples were composed mainly of kaolinite and hematite with little nontronite. The (060) reflection of kaolinite occurred at 1.49 Å (Figure 2b), which corresponded to the Al-infilling oxygen octahedral sheets of kaolinite. Accordingly, the Stage III samples, *e.g.*, $N_{Au\text{-}96h}$, showed well-crystallized kaolinite layers (Figure 3d).

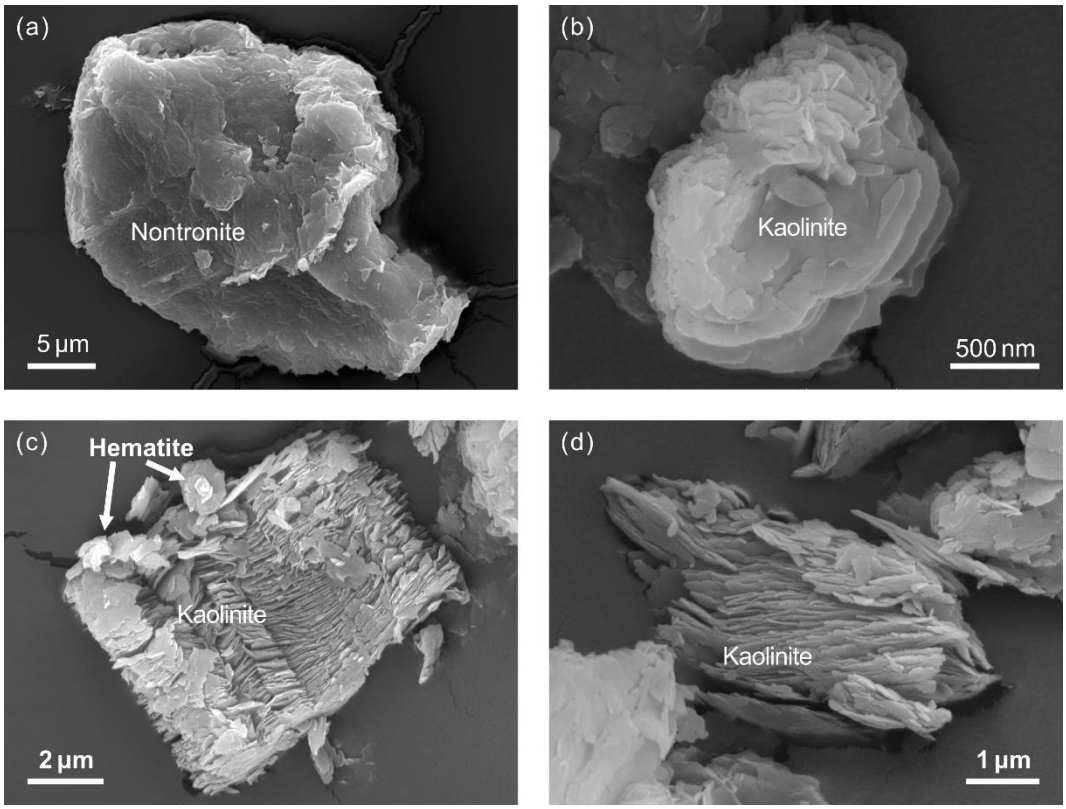

Figure 3. Scanning electron microscopic images of different stages of kaolinized nontronite. (a) nontronite particle in sample N_{Au}; (b) kaolinite particle in sample $N_{Au\text{-}24h}$; (c) kaolinite and hematite particle in sample $N_{Au\text{-}48h}$; and (d) kaolinite particle in sample $N_{Au\text{-}96h}$.

4.2 Hydroxyl (OH) and water molecule (H_2O) contents

Nontronite generally showed significant mass losses in the range from room temperature to ca. 300 ℃, which originates from loss of interlayer water associated with

interlayer cations (*e.g.*, K^+, Na^+, and Ca^{2+}). Significant mass losses at temperature above 300 ℃ can be attributed to dehydroxylation of clay minerals (He et al., 2017; Li et al., 2020; Zhang et al., 2017). Accordingly, the OH and H_2O contents of the three stages of samples can be quantified using the TG analysis based on the mass loss caused by dehydration and dehydroxylation (Figure 4).

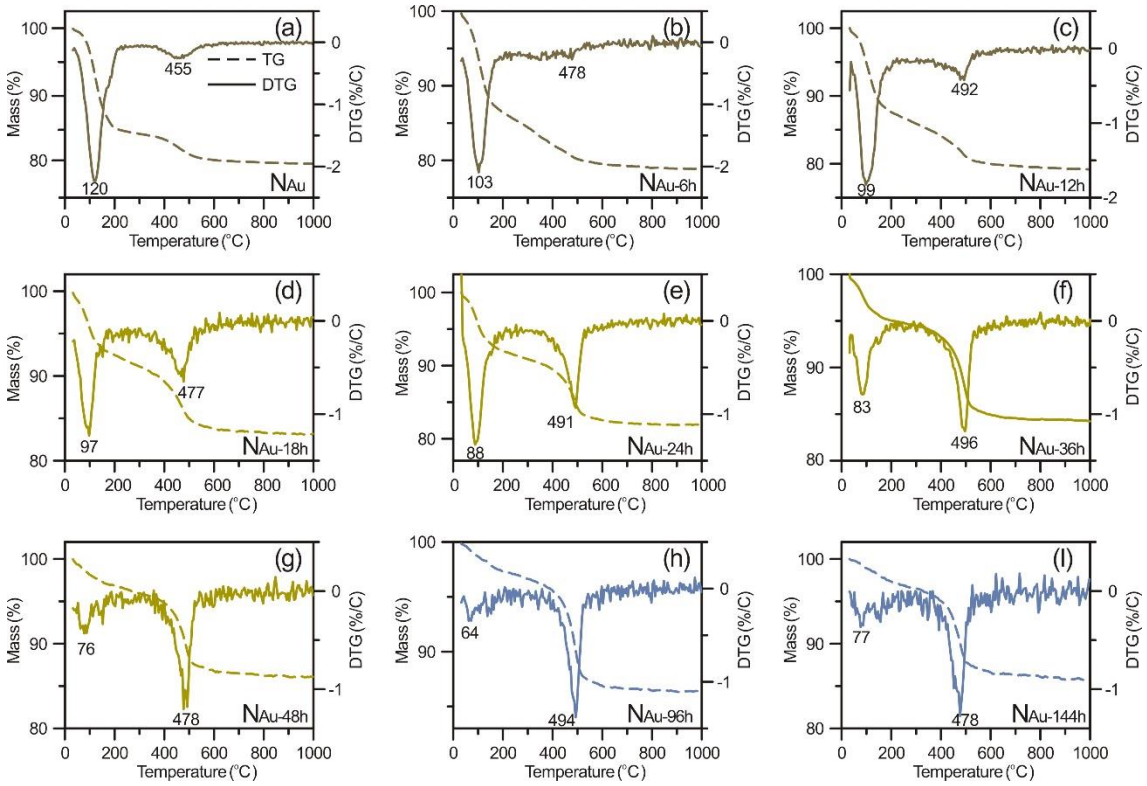

Figure 4. TG and DTG curves collected from different stages of kaolinized nontronite. The solid line is the curves of DTG and the dashed line is the curves of TG. The colors of TG and DTG curves correspond to the sample stage colors in Figure 2.

The TG and DTG curves of the Stage I samples showed two major mass losses at 100–120 ℃ and 455–500 ℃ (Figures 4a-c), corresponding to the dehydration and dehydroxylation temperatures of nontronite, respectively (Ding & Frost, 2002). In general, the Stage I samples had a higher dehydration temperature (Figures 4a-c). The

Stage I samples generally lost about 15 wt.% mass at 30–300 ℃ due to dehydration, and about 6 wt.% mass at 300–700 ℃ due to dehydroxylation (Figures 4a-c).

The Stage II samples generally had a lower dehydration temperature compared to the Stage I samples. In particular, the TG and DTG curves of the Stage II samples showed significant mass loss at about 90 and 500 ℃ (Figures 4d-g), corresponding to the dehydration and dehydroxylation temperatures of the nontronite and kaolinite mixture. As the transformation of nontronite to kaolinite progressed, the dehydration temperatures gradually decreased from 97 to 76 ℃ and the main dehydroxylation temperature occurred at ~500 ℃. Calculations showed that the mass losses of dehydration were 4–10 wt.% and the mass losses of dehydroxylation were 7–10 wt.% (Figures 4d-g).

The Stage III samples had different dehydration temperatures and mass losses during dehydration and dehydroxylation compared to the Stage II samples. The TG and DTG curves of the samples from the Stage III showed two prominent mass loss temperatures at ~64 and ~500 ℃ (Figures 4h-I), corresponding to the dehydration and dehydroxylation of kaolinite, respectively. In addition, the samples from the Stage III exhibited ~3 wt.% mass loss due to dehydration at 30–300 ℃ and ~10 wt.% mass losses due to dehydroxylation at 300–700 ℃ (Figures 4h-I).

4.3 VNIR spectra of kaolinized nontronite

VNIR spectroscopy (350–2500 nm) includes the visible (350–1000 nm) and near infrared (1000–2500 nm) regions (Hunt, 1977; Hunt & Ashley, 1979). In this study, the absorption bands at 350–1000 nm are likely due to the electronic transitions of Fe^{3+} in

nontronite and hematite. The absorption bands at 1000–2500 nm corresponded to the overtone and combination of water and metal-OH (metal=Al, Fe and Mg) in nontronite and kaolinite (Bishop et al., 2002, 2008; Cuadros et al., 2016; Fox et al., 2021).

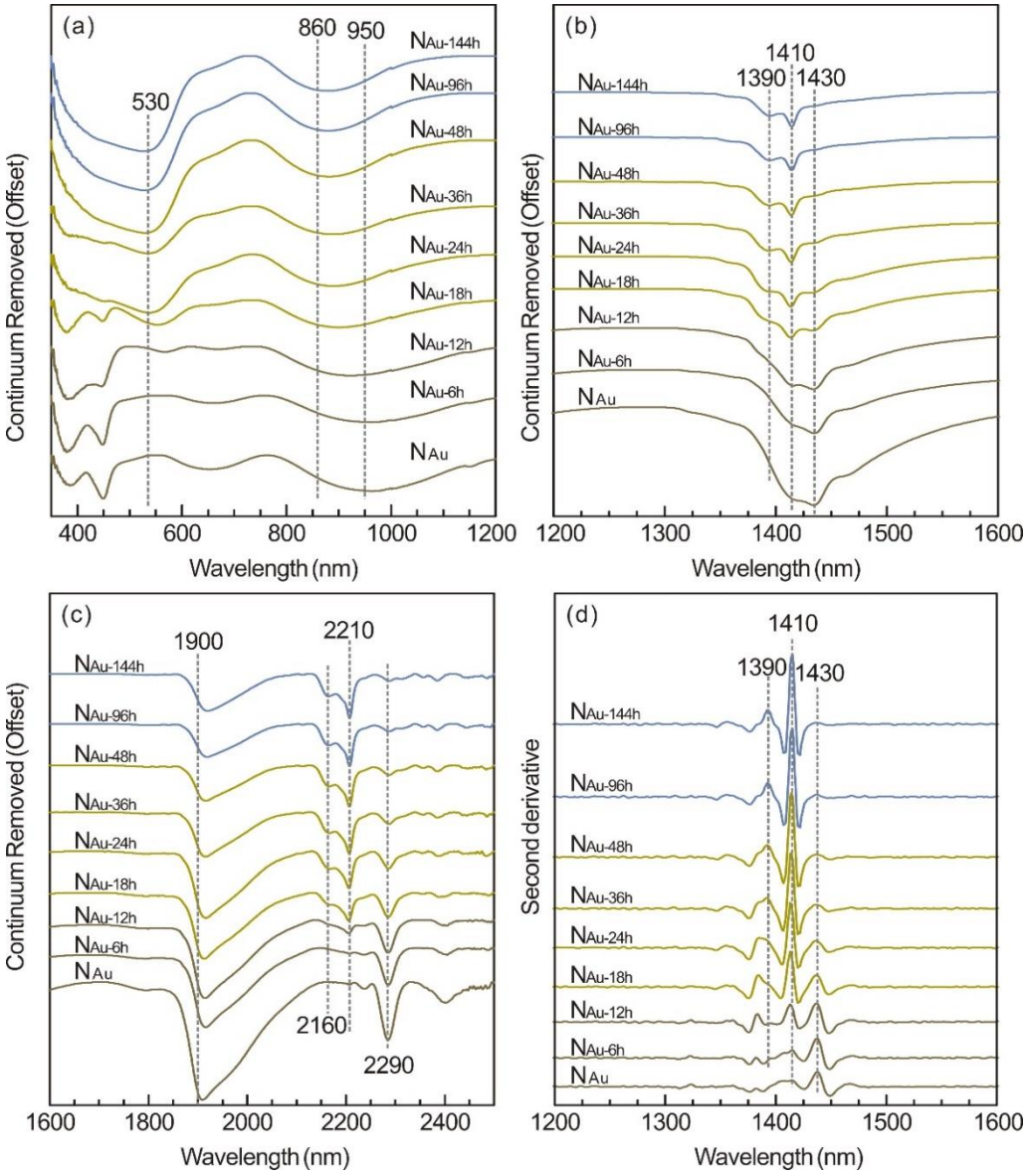

Figure 5. Visible/near-infrared reflectance spectra of different stages of kaolinized nontronite. (a) Continuum-removed reflectance spectra of Fe-related bands within the range of 350-1200 nm; (b) Continuum-removed reflectance spectra of OH at the band of 1200–1600 nm; (c) Continuum-removed reflectance spectra at the band of 1600–2500 nm, and show a decrease trend of the absorption band at 1900 nm (d) Second derivative curves of OH at the band of 1200–1600 nm and show an increase trend of the absorption band at 1410 nm. The spectra have been offset for clarity but are shown on a common scale for band intensity comparison. The colors of spectral curves correspond to the sample stage colors, referring to figure 2.

292 Spectra of the Stage I samples showed characteristic absorptions of nontronite at
293 ~950, ~1430, ~1900 and ~2290 nm (Figure 5a). The absorption at ~950 nm
294 corresponded to the Fe^{3+} electronic transitions of nontronite. The absorption at ~1430
295 nm was the first overtone of the $Fe^{3+}Fe^{3+}$-OH stretching of nontronite. The band at
296 ~1900 nm corresponded to a combination of stretching and bending vibrations of the
297 interlayer H_2O. Furthermore, the absorption at ~2290 nm was from the combination of
298 stretching and bending vibrations of $Fe^{3+}Fe^{3+}$-OH and was the diagnostic absorption of
299 nontronite (Bibring et al., 2005; Bishop et al., 2008; Ehlmann et al., 2009). The
300 absorption depth at ~2290 nm of the samples gradually decreased with progressive
301 transformation of nontronite to kaolinite (Figure 5c).
302 The Stage II samples showed additional characteristic absorptions at ~1390, ~1410,
303 ~2160 and ~2210 nm (Figures 5b-c). The absorptions at ~1390 and ~1410 nm were
304 derived from the first overtone of AlAl-OH stretching, and the absorptions at ~2160
305 and ~2210 nm can be attributed to the combination of stretching and bending vibrations
306 of AlAl-OH in kaolinite. The Stage II samples also showed characteristic absorption of
307 hematite at ~530 and ~860 nm, which can be attributed to electron transitions from Fe^{3+}.
308 As the transformation of nontronite to kaolinite progressed, the Stage II samples
309 showed a gradual increase in the absorption intensity of hematite at ~530 nm and
310 kaolinite at ~1410 nm (Figures 5a & d). Correspondingly, the absorption of nontronite,
311 *e.g.*, at ~1430 nm, was gradually weakened (Figure 5d).
312 The absorption of nontronite (*e.g.*, ~1430 nm) in the Stage III samples was further
313 weakened and disappeared (Figure 5d), while the absorption of kaolinite and hematite

was gradually enhanced (Figure 5). Specifically, the Stage III samples showed the absorption of hematite at ~530 and ~860 nm and that of kaolinite at ~1390, ~1410, ~2160 and ~2210 nm.

5 Discussion

5.1. Transformation of nontronite to kaolinite in basaltic weathering successions

Weathering of basalt is dominated by the surface process of top-down leaching, which leads to decomposition of rock-forming minerals (*e.g.*, olivine and pyroxene) and subsequent formation of secondary minerals (*e.g.*, nontronite and kaolinite) (Liu et al., 2021a; Nahon et al., 1982). Chemical reactions between water and basalt tend to convert anhydrous materials, *e.g.*, olivine and pyroxene, to the clay mineral nontronite of type 2:1 at the stage of early weathering, by leaching composition elements (*e.g.*, Ca, Mg and Si) and inducing OH and H_2O (Cuadros & Michalski, 2013; Ehlmann et al., 2011b; Nahon et al., 1982; Wilson, 2004). H_2O tends to form complexes with interlayer cations (*e.g.*, K^+, Na^+, Ca^{2+}) within the interlayer sites of nontronite, whereas OH is likely bound to the Al/Fe/Mg-O octahedral sheet of nontronite (Cuadros & Michalski, 2013).

In the context of the weathering profile, nontronite is a transient phase that forms in weathered rocks (Wilson, 2004). Basaltic weathering successions generally show a gradual increase in the amount of kaolinite from bottom to top due to progressive weathering, as evidenced by the transitional zones containing different proportions of nontronite and kaolinite in basaltic weathering successions formed under warm

climates (Gaudin et al., 2011; Prudencio et al., 2002). During the transformation of nontronite to kaolinite, more OH is incorporated into the clay mineral structure by hydrolysis, while H_2O in the interlayer, cations, and Si-O tetrahedral sheets tend to be gradually leached (Li et al., 2020). As a result, the transformation of nontronite to kaolinite mainly involves changes in the OH/H_2O and Si/Al ratios in the clay minerals, which are essentially positively correlated with the weathering intensity of a basaltic weathering succession (Liu et al., 2021a).

5.2. Change of H_2O and OH content in the transformation of nontronite to kaolinite

Sustained leaching of Si from nontronite lowers the Si/Al ratio in the mineral-water reaction system, facilitating the transformation of nontronite to kaolinite. In the present study, a similar transformation process is modeled experimentally by lowering the Si/Al ratio of the nontronite-water reaction system with external Al^{3+}. With increased reaction time, the initial mineral nontronite is gradually transformed into a mixture of nontronite and kaolinite, and finally to kaolinite (Figures 2 & 3), which is consistent with clay mineral transformation in a basaltic weathering succession (Gaudin et al., 2011; Liu et al., 2021a; Prudencio et al., 2002).

In the transformation of nontronite to kaolinite, nontronite is the main host of H_2O bound with its interlayer cations, whereas kaolinite contains few interlayer cations and H_2O (Cuadros, 1997; Ding & Frost, 2002; Fernandez-Caliani et al., 2004; Fox et al., 2021; Pineau et al., 2022). Analysis of TG shows that the H_2O concentration of the transformation products gradually decreases from ~15 wt.% in the Stage I samples to

4–10 wt.% in the Stage II samples and to ~3 wt.% in Stage III samples (Figure 4 and Figure 6a). Furthermore, the dehydration temperature systematically shifts to lower temperatures as the transformation of nontronite to kaolinite progresses, from 100–120 ℃ in the Stage I samples to ~76–97 ℃ in the Stage II samples, and finally to ~64 ℃ in Stage III samples (Figure 4 and Figure 6b). The decrease in dehydration temperature indicates that less energy is required to break the hydrogen bond between the H_2O molecules in the nontronite (Madejová et al., 2002), corresponding to a decrease in the abundance of nontronite in the transformation products (Figure 2&3). Thus, the decrease in H_2O content is consistent with the abundance of nontronite during the progressive transformation of nontronite into kaolinite.

The transformation of nontronite to kaolinite also leads to significant changes in the OH content of the different stages of kaolinized nontronite. The kaolinite has 8 hydroxyl groups per complete structural formula, whereas nontronite has only 4 hydroxyl groups (Cuadros et al., 2019; Li et al., 2020). Thus, one half of the Si-O tetrahedral sheets should be lost and hydroxyl groups induced when nontronite transforms to kaolinite. The analyses of TG show that the content of OH gradually increases from ~6 wt.% to ~10 wt.% as the transformation of nontronite to kaolinite progresses (Figure 4 and Figure 6c). Thus, the increase in OH content is consistent with the abundance of kaolinite during the progressive transformation of nontronite into kaolinite.

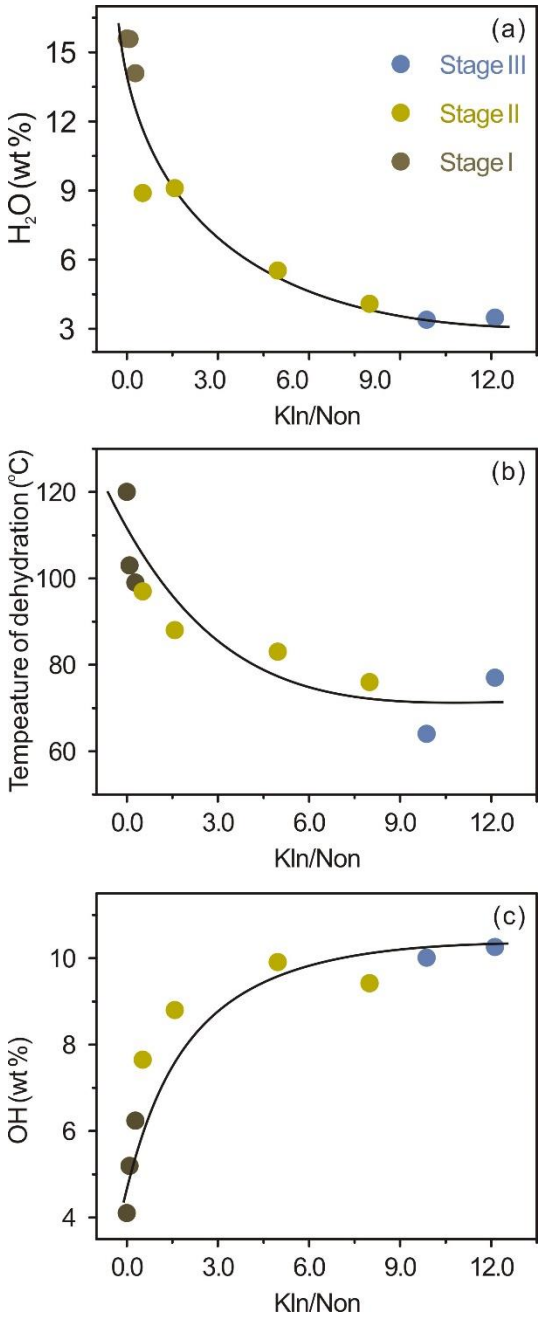

Figure 6. Change of H_2O and OH content in the transformation of nontronite to kaolinite. (a) The mass losses of dehydrations of different stages of nontronite → kaolinite transformation products; (b) The dehydrations temperature of different stages of nontronite → kaolinite transformation products; and (c) The mass losses of dehydroxylations in different stages of nontronite → kaolinite transformation products.

5.3. Spectral proxies for kaolinized nontronite

Previous studies suggest that interlayer cations and the amount of interlayer water determine the VNIR spectral features at band of 1900 nm (Bishop et al., 1994).

Nevertheless, interlayer cations of clay minerals only have indirect effects on ~1900 nm absorption by affecting the amount of H_2O molecules bound on them (Bishop et al., 1994). In the present study, the band depth at ~1900 nm (BD1900) gradually decreases as the transformation of nontronite to kaolinite progresses (Figure 5c). Remarkably, BD1900 shows a positive linear correlation (R^2=0.82) with the H_2O content in the different stages of kaolinized nontronite (Figure 7a). Since nontronite is the major host of H_2O, the BD1900 can serve as an effect spectral proxy to quantify the abundance of nontronite in the transformation products.

The band position of OH absorption at 1400 nm is affected by the electronegativity and ionic radius of the octahedral cations (Mart ńez-Alonso et al., 2002). The VNIR absorption at ~1400 nm possible includes three bands originating from metal-OH vibrations in kaolinite and nontronite, *i.e.*, 1390 nm, 1410 nm, and 1430 nm (Figure 5b&d). The band at 1390 nm originates from the first overtone of inner-surface hydroxyl groups' stretching vibration of AlAl-OH in kaolinite, the band at 1410 nm originated from the first overtone of inner hydroxyl groups' stretching vibration of AlAl-OH in kaolinite (Tan et al., 2022), and the band at near 1430 nm derived from stretching vibration of $Fe^{3+}Fe^{3+}$-OH in nontronite (Bishop et al., 2008; Ehlmann et al., 2009). Therefore, the band depths at 1390 and 1410 nm tend to increase, while the band depth at 1430 nm decreases as the transformation of nontronite to kaolinite progresses (Figures 5b & d). As a result, the band depth at ~1400 nm (BD1400) poorly correlates with the concentrations of OH in the different stages of kaolinized nontronite, due to the interference of the three bands (Figure 7b). In contrast, the spectral proxy

H1410_2nd (height of second derivative curves at the band of 1410 nm) gradually increases (Figure 5d) and shows a positive linear correlation (R^2=0.96) with the content of OH in the kaolinized nontronite (Figure 7c).

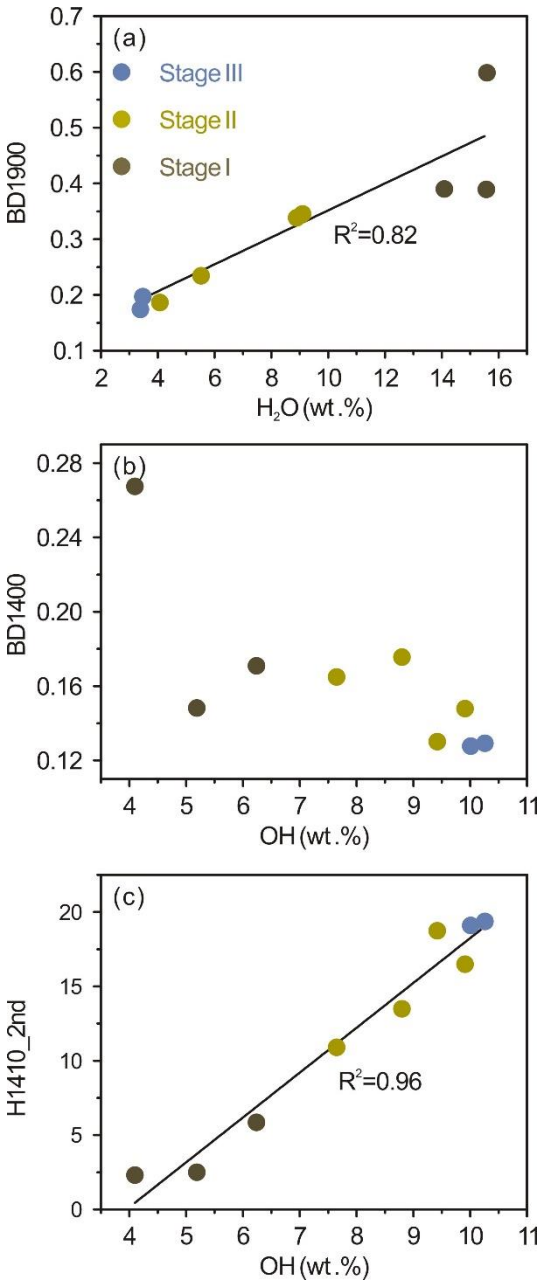

Figure 7. Spectral proxies of H_2O and OH content in the nontronite → kaolinite transformation. (a) Plots of the spectral parameters BD1900 versus H_2O content; (b) Plots of the spectral parameters BD1400 versus OH content; and (c) Plots of the spectral parameters H1410_2nd versus OH content.

5.4 Spectral proxies for weathering intensity of basaltic successions

Progressive chemical weathering of terrestrial basalt results in replacement of nontronite with kaolinite, leading to an increase in OH content and a concomitant decrease in H_2O content (Figure 4&6). Thus, the ratio of OH to H_2O content is essentially related to the weathering intensity of a basaltic weathering succession and increases gradually (Figure 8a). The present study has shown that the content of H_2O and OH can be quantitatively assessed by the spectral proxies BD1900 (Figure 7a) and H1410_2nd (Figure 7c), respectively. In particular, the ratio of H1410_2nd to BD1900 (H1410_2nd/BD1900) shows a strong positive correlation (R^2=0.98) with weathering intensity (OH/H_2O, Figure 8b) and the abundance ratio of kaolinite to nontronite (Kln/Non, Figure 8c). Therefore, the weathering intensity of a basaltic weathering succession can be well estimated by the spectral proxy H1410_2nd/BD1900 (Figure 8c; R^2=0.91).

Specifically for CRISM spectra collected from the surface of Mars, the data set has a relatively low signal-to-noise ratio (Pineau et al., 2022; Zhang et al., 2022) and is characterized by weak and broad absorption (Cuadros et al., 2016). As a result, the absorption at the 1390 nm, 1410 nm, and 1430 nm can hardly be resolved, and it is unreasonable to use H1410_2nd/BD1900 to quantitatively constrain the weathering intensities of a basaltic weathering succession on Mars. Nevertheless, photooxidation may have affected the Fe-clay minerals formed near the surface and caused the absorption of $Fe^{3+}Fe^{3+}$-OH to disappear at ~1400 nm (Rivera Banuchi et al., 2022). The absorption band at ~1400 nm is likely caused by AlAl-OH of kaolinite on Mars, so

BD1400 is likely effective for characterizing the OH content of kaolinite on Mars. Given that the ratio of BD1400 to BD1900 (BD1400/BD1900) also demonstrates a reasonable positive correlation with the abundance ratio of kaolinite to nontronite (Figure 8d; R^2=0.83), the BD1400/BD1900 can serve as a good indication of weathering intensity in the basaltic weathering succession on Mars.

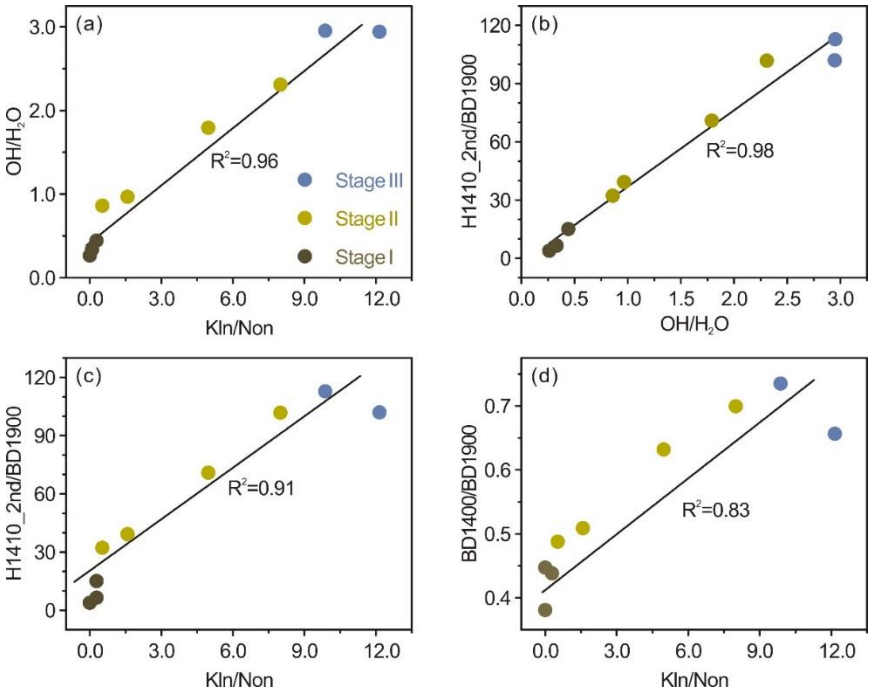

Figure 8. Spectral proxies for weathering intensity of basaltic succession. (a) Plots of the abundance ratio of OH to H_2O (OH/H_2O) versus the abundance ratio of kaolinite (Kln) to nontronite (Non) (Kln/Non); (b) Plots of H1410_2nd/BD1900 versus the weathering intensity proxy OH/H_2O; (c) Plots of H1410_2nd/BD1900 versus Kln/Non and (d) Plots of BD1400/BD1900 versus Kln/Non.

5.5. Analogue spectra of the compositional stratigraphy on Mars

The main debate about the genesis of compositional stratigraphy on the Martian surface is whether the clay minerals changed through chemical weathering (Bibring et al., 2006; Bishop et al., 2018; Carter et al., 2015; Ehlmann et al., 2013; Liu et al., 2021b; Ye & Michalski, 2021) or formed by deposition of various sediments (Bishop et al.,

2020; Ehlmann et al., 2013; Lowe et al., 2020; Michalski et al., 2013). This study provides spectral parameters collected from different stages of kaolinized nontronite, *e.g.*, BD1400, BD1900 and BD1400/BD1900, to investigate the content of OH, H_2O, and weathering intensity of the different units consisting compositional stratigraphy on Mars, which could provide crucial clues to the genesis of compositional stratigraphy.

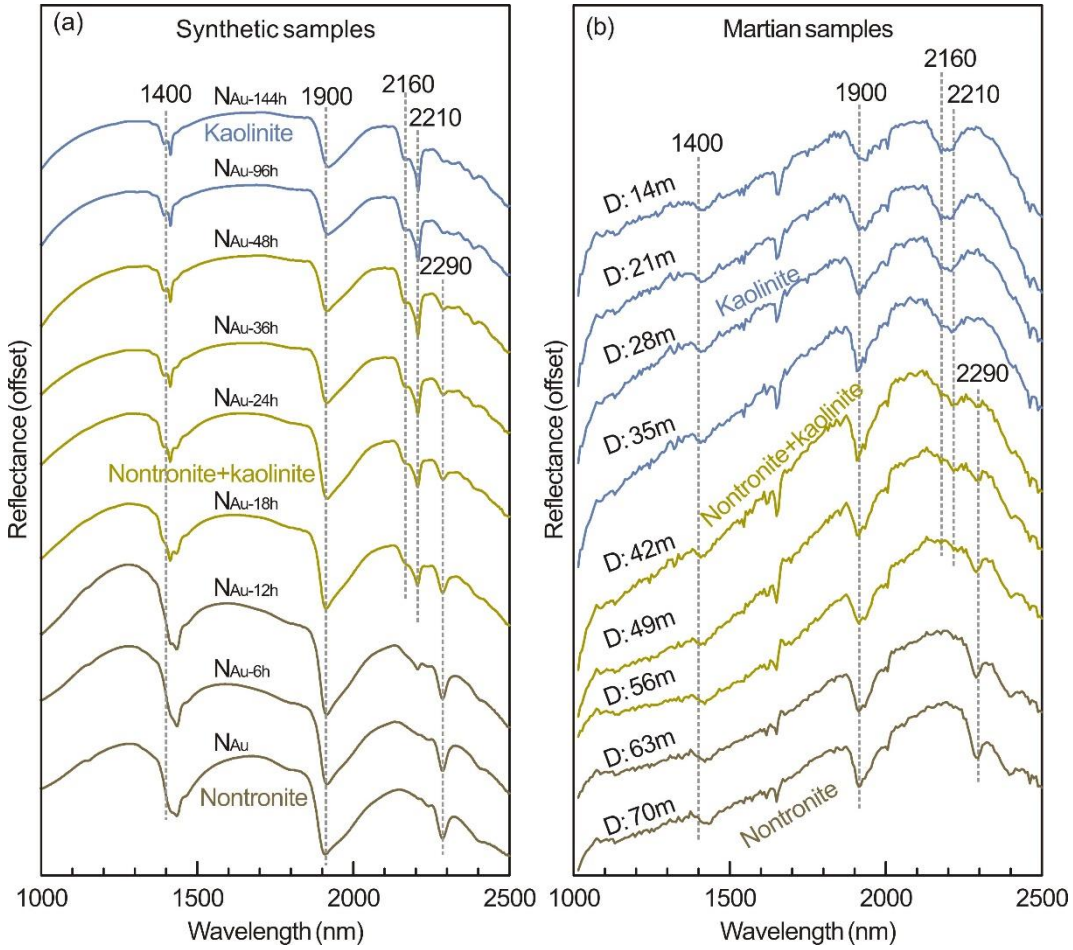

Figure 9. Comparison between the reflectance spectra of the nontronite → kaolinite transformation products with the CRISM spectra collected from a compositional stratigraphy on Mars. (a) The spectra of sample N_{Au} and its transformed products; (b) the CRISM spectra from the different depths of a compositional stratigraphy on Mars (the data on which this figure is based are available in Liu et al., 2021b), and D is depth of the thick clays profile.

Spectra from the α1 zone of the compositional stratigraphy on Mars show absorption bands at ~1400, ~1900, and ~2290 nm (Figure 9b). The band positions of

471 these absorptions are consistent with those of nontronite from Stage I samples in the
472 laboratory (Figure 9a) and the absorption at ~2290 nm is the diagnostic absorption of
473 nontronite (Bibring et al., 2005), suggesting that nontronite, is the dominant mineral in
474 the α1 zone.

475 In the α2 zone of the compositional stratigraphy, the spectra have absorptions at
476 ~1400, ~1900, ~2200 and ~2290 nm (Figure 9b). The band positions of these
477 absorptions are consistent with those of the Stage II kaolinized nontronite (Figure 9a).
478 The band asymmetry of the ~2200 absorption gradually shift toward the short
479 wavelength side, indicating the presence of kaolinite (Bibring et al., 2005). As a result,
480 the α2 zone of the compositional stratigraphy represent a mixture of nontronite and
481 kaolinite.

482 Moreover, BD1900 gradually decreases while BD1400 gradually increases from
483 bottom to top in the α2 zone (Figure 10b), which is exactly consistent with the
484 transformation of the samples of the Stage II (Figure 10a). This shows that hydroxyl
485 and leaching gradually increase upward. In addition, BD1400/BD1900 shows a
486 consistent increasing trend from the bottom to top in the Martian profile (Figure 10b),
487 which is accordant with the progressive transformation of nontronite to kaolinite
488 (Figure 10a). These variation trends in spectral proxies along the compositional
489 stratigraphy from bottom to top reflect the gradual decomposition of nontronite and
490 formation of kaolinite with increasing weathering intensity, by relating to the
491 experimentally modeled transformation of nontronite to kaolinite.

492

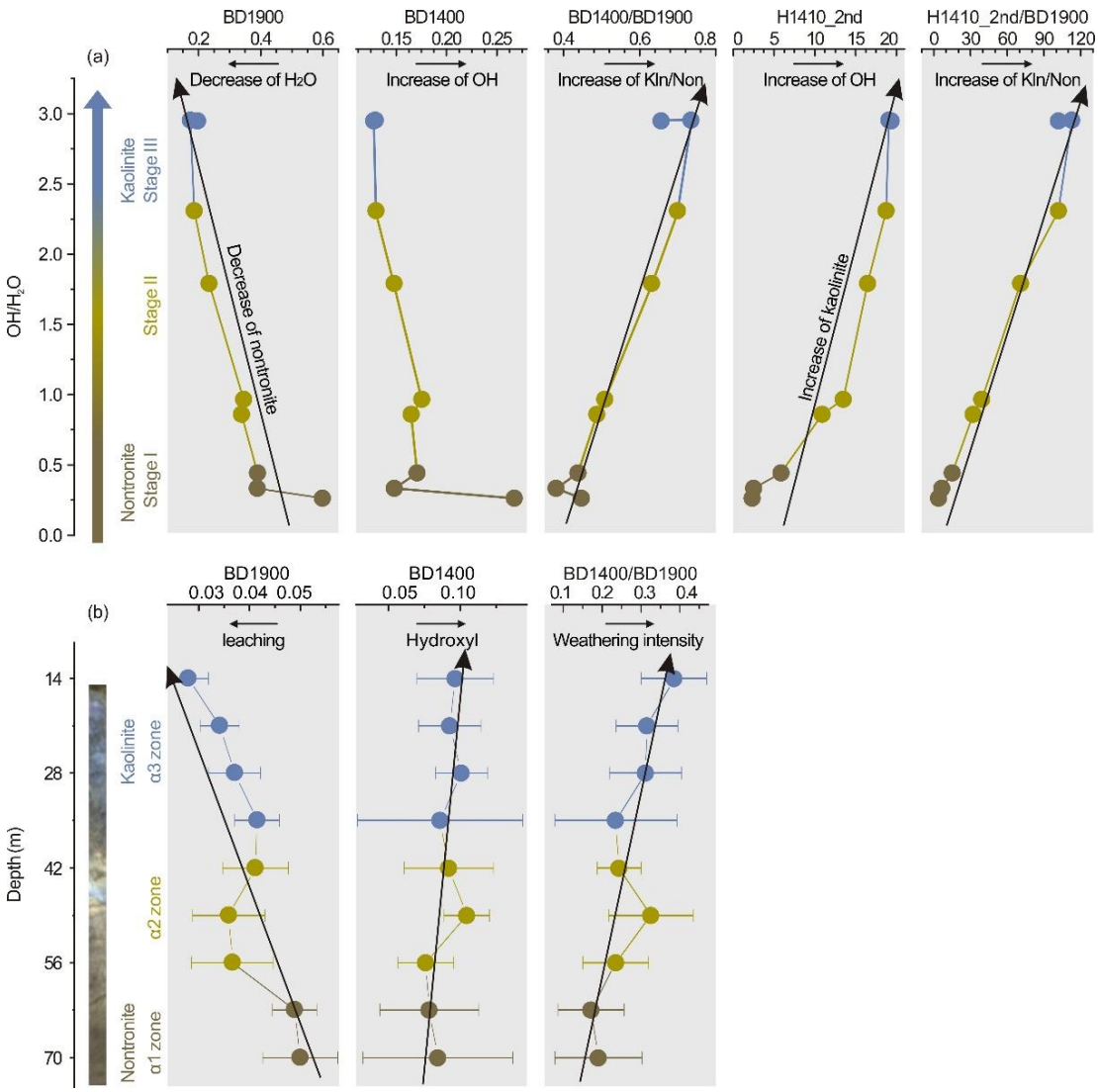

Figure 10. Variation trends of the spectral parameters of different stages of kaolinized nontronite and a compositional stratigraphy in the Mawrth Vallis region, Mars. (a) Variation of the spectral parameters BD1900, BD1400, BD1400/BD1900, H1410_2nd and H1410_2nd/BD1900 in the progressive transformation of nontronite to a mixture of nontronite and kaolinite, and finally to kaolinite; (b) The variation of the spectral parameters BD1900, BD1400 and BD1400/BD1900 along the compositional stratigraphy on Mars (the data on which this figure is based are available in Liu et al., 2021b).

The spectra from the α3 zone show absorptions at ~1400 and ~1900 nm and a doublet at ~2200 nm while the absorption at ~2290 nm disappears (Figure 9b). The band positions of these absorptions are consistent with those of kaolinite from experimentally modeled Stage III samples (Figure 9a). The doublet at ~2200 nm is the

506 diagnostic absorption of kaolinite, indicating that kaolinite becomes the dominant phase
507 in the α3 zone.

508 These observed variation trends in CRISM spectra reflect evolutionary features of
509 both mineral composition and weathering intensity in the compositional stratigraphy of
510 Mars (Figure 10). In particular, the variation trends of BD1900, BD1400 and
511 BD1400/BD1900 continue from the α1 zone to the α3 zone in the compositional
512 stratigraphy (Figure 10b), corresponding to a progressive conversion of nontronite to
513 kaolinite by chemical weathering from top to bottom. Such continuous variation trends
514 can hardly be achieved by the stratigraphic deposition of detrital phyllosilicate
515 sediments, which are likely to exhibit irregular fluctuations in mineral composition and
516 weathering intensity due to the unpredictable origin of the sediments and abrupt
517 changes in protolithic minerals (Liu et al., 2021a; Tan et al., 2022). Thus, the
518 compositional stratigraphy on Mars may have been formed by a top-down chemical
519 weathering process. It is possible that Mars had a warm and wet climate capable of
520 maintaining liquid water on the surface over geologic time and the compositional
521 stratigraphy formed through the ongoing reaction between the liquid water and the
522 primary minerals in basalt.

523

524 **6 Conclusions**

525 The transformation of nontronite to kaolinite is modeled experimentally and
526 studied quantitatively using TG and VNIR to test the effectiveness of spectral proxies
527 for mineral evolution and weathering intensity in a basaltic succession. Analysis of TG

shows that the H_2O content gradually decreases, while OH gradually increases with the progressive transformation of nontronite to kaolinite. Thus the ratio of OH/H_2O is positively correlated with the weathering intensity of a basaltic weathering succession. The present study demonstrates the effectiveness of BD1900, H1410_2nd, H1410_2nd /BD1900 and BD1400/BD1900 as spectral proxies for H_2O content, OH content, and weathering intensity during the conversion of nontronite to kaolinite in a basaltic weathering succession. The obtained results allow us to reveal the genesis of compositional stratigraphy on Mars. The continuous trends of BD1900, BD1400 and BD1400/BD1900 indicate a progressive transformation of nontronite into a mixture of nontronite and kaolinite, and finally into kaolinite. Accordingly, the compositional stratigraphy on Mars may have been formed by a progressive chemical weathering process from top to bottom. Thus, the formation of the compositional stratigraphy suggests that Mars had a warm and wet climate that could hold liquid water on its surface over geologic time span.

Acknowledgement

This work was financially supported by the National Natural Science Foundation of China (Grant No. 41921003; 41825003; 42072044), Department of Science and Technology of Guangdong Province (Grant No.2017GC010578), and the Science and Technology Planning Project of Guangdong Province, China (2020B1212060055).

Data Availability Statement

CRISM hyperspectral data and HiRISE image used in this work are available via the Planetary Data System (https://pds.nasa.gov). The mineralogical and VNIR spectroscopic characteristics of different stages of kaolinized nontronite is available in an external repository via https://data.mendeley.com/datasets/ws34469r9x. ViewSpecPro software (version 6.0) provided by ASD Inc. was used to process the original VNIR spectral data.

References

Bibring, J. P., Langevin, Y., Gendrin, A., Gondet, B., Poulet, F., Berthé, M., et al. (2005). Mars surface diversity as revealed by the OMEGA/Mars Express observations. *Science*, *307*(5715), 1576-1581. https://doi.org/10.1126/science.1108806

Bibring, J. P., Langevin, Y., Mustard, J. F., Poulet, F., Arvidson, R., Gendrin, A., et al. (2006). Global mineralogical and aqueous Mars history derived from OMEGA/Mars express data. *Science*, *312*(5772), 400-404.

https://doi.org/10.1126/science.1122659

Bishop, J., Madejová, J., Komadel, P., & Fröschl, H. (2002). The influence of structural Fe, Al and Mg on the infrared OH bands in spectra of dioctahedral smectites. *Clay Minerals*, *37*(4), 607-616. https://doi.org/10.1180/0009855023740063

Bishop, J. L., Fairén, A. G., Michalski, J. R., Gago-duport, L., Baker, L. L., Velbel, M. A., et al. (2018). Surface clay formation during short-term warmer and wetter conditions on a largely cold ancient Mars. *Nature Astronomy*, *2*(3), 260-213. https://doi.org/10.1038/s41550-017-0377-9

Bishop, J. L., Gross, C., Danielsen, J., Parente, M., Murchie, S. L., Horgan, B., et al. (2020). Multiple mineral horizons in layered outcrops at Mawrth Vallis, Mars, signify changing geochemical environments on early Mars. *Icarus*, *341*, 113634. https://doi.org/10.1016/j.icarus.2020.113634

Bishop, J. L., Lane, M. D., Dyar, M. D., & Brown, A. J. (2008). Reflectance and emission spectroscopy study of four groups of phyllosilicates: Smectites, kaolinite-serpentines, chlorites and micas. *Clay Minerals*, *43*(1), 35-54. https://doi.org/10.1180/claymin.2008.043.1.03

Bishop, J. L., Pieters, C. M., & Edwards, J. O. (1994). Infrared spectroscopic analyses on the nature of water in montmorillonite. *Clays and Clay Minerals*, *42*(6), 702-716. https://doi.org/10.1346/ccmn.1994.0420606

Bristow, T. F., Grotzinger, J. P., Rampe, E. B., Cuadros, J., Chipera, S. J., Downs, G. W., et al. (2021). Brine-driven destruction of clay minerals in Gale crater, Mars. *Science*, *373*(6551), 198-204. https://doi.org/10.1126/science.abg5449

587 Carter, J., Loizeau, D., Mangold, N., Poulet, F., & Bibring, J. (2015). Widespread
588 surface weathering on early Mars: A case for a warmer and wetter climate. *Icarus*,
589 *248*, 373-382. https://doi.org/10.1016/j.icarus.2014.11.011
590 Carter, J., Poulet, F., Bibring, J. P., Mangold, N., & Murchie, S. (2013). Hydrous
591 minerals on Mars as seen by the CRISM and OMEGA imaging spectrometers:
592 Updated global view: Hydrous minerals on Mars: Global view. *Journal of*
593 *Geophysical Research: Planets*, *118*(4), 831-858.
594 https://doi.org/10.1029/2012JE004145
595 Chauviré, B., Pineau, M., Quirico, E., & Beck, P. (2021). Near infrared signature of
596 opaline silica at Mars-relevant pressure and temperature. *Earth and Planetary*
597 *Science Letters*, *576*(15), 117239. https://doi.org/10.1016/j.epsl.2021.117239
598 Cuadros, J. (1997). Interlayer cation effects on the hydration state of smectite. *American*
599 *Journal of Science*, *297*, 829-841. https://doi.org/10.2475/ajs.297.8.829
600 Cuadros, J., Mavris, C., Michalski, J. R., Nieto, J. M., Bishop, J. L., & Fiore, S. (2019).
601 Abundance and composition of kaolinite on Mars: Information from NIR spectra
602 of rocks from acid-alteration environments, Riotinto, SE Spain. *Icarus*, *330*(15),
603 30-41. https://doi.org/10.1016/j.icarus.2019.04.027
604 Cuadros, J., & Michalski, J. R. (2013). Investigation of Al-rich clays on Mars: Evidence
605 for kaolinite–smectite mixed-layer versus mixture of end-member phases. *Icarus*,
606 *222*(1), 296-306. https://doi.org/10.1016/j.icarus.2012.11.006
607 Cuadros, J., Michalski, J. R., Dekov, V., & Bishop, J. L. (2016). Octahedral chemistry
608 of 2:1 clay minerals and hydroxyl band position in the near-infrared: Application

609 to Mars. *American Mineralogist*, *101*(3), 554-563. https://doi.org/10.2138/am-
610 2016-5366
611 Ding, Z., & Frost, R. L. (2002). Controlled rate thermal analysis of nontronite.
612 *Thermochimica Acta*, *389*(1-2), 185-193. https://doi.org/10.1016/ S0040-
613 6031(02)0059-X
614 Ehlmann, B. L., Berger, G., Mangold, N., Michalski, J. R., Catling, D. C., Ruff, S. W.,
615 et al. (2013). Geochemical consequences of widespread clay mineral formation in
616 Mars' ancient crust. *Space Science Reviews*, *174*(1 - 4), 329–364.
617 https://doi.org/10.1007/s11214-012-9930-0
618 Ehlmann, B. L., Mustard, J. F., Clark, R. N., Swayze, G. A., & Murchie, S. L. (2011a).
619 Evidence for low-grade metamorphism, hydrothermal alteration, and diagenesis
620 on Mars from phyllosilicate mineral assemblages. *Clays and Clay Minerals*, *59*(4),
621 359-377. https://doi. org/10.1346/ccmn.2011.0590402
622 Ehlmann, B. L., Mustard, J. F., Murchie, S. L., Bibring, J. P., Meunier, A., Fraeman, A.
623 A., & Langevin, Y. (2011b). Subsurface water and clay mineral formation during
624 the early history of Mars. *Nature*, *479*(7371), 53-60.
625 https://doi.org/10.1038/nature10582
626 Ehlmann, B. L., Mustard, J. F., Swayze, G. A., Clark, R. N., Bishop, J. L., Poulet, F., et
627 al. (2009). Identification of hydrated silicate minerals on Mars using MRO-
628 CRISM: Geologic context near Nili Fossae and implications for aqueous alteration.
629 *Journal of Geophysical Research*, *114*(E2), E00D08.
630 https://doi.org/10.1029/2009JE003339

631 Fernandez-Caliani, J. C., Crespo, E., Rodas, M., Barrenechea, J. F., & Luque, F. J.
632 (2004). Formation of nontronite from oxidative dissolution of pyrite disseminated
633 in precambrian felsic metavolcanics of the Southern Iberian Massif (Spain). *Clays*
634 *and Clay Minerals*, *52*, 106-114. https://doi.org/10.1346/CCMN.2004.0520110
635 Fox, V. K., Kupper, R. J., Ehlmann, B. L., Catalano, J. G., Razzell-Hollis, J., Abbey, W.
636 J., et al. (2021). Synthesis and characterization of Fe(III)-Fe(II)-Mg-Al smectite
637 solid solutions and implications for planetary science. *American Mineralogist*,
638 *106*(6), 964-982. https://doi. org/10.2138/am-2020-7419CCBYNCND
639 Frost, R. L., Kloprogge, J. T., & Ding, Z. (2002). The Garfield and Uley nontronites -
640 an infrared spectroscopic comparison. *Spectrochimica Acta Part A-Molecular and*
641 *Biomolecular Spectroscopy*, *58*, 1881-1894. https://doi.org/10.1016/S1386-
642 1425(01)00638-2
643 Gainey, S. R., Hausrath, E. M., Hurowitz, J. A., & Milliken, R. E. (2014). Nontronite
644 dissolution rates and implications for Mars. *Geochimica et Cosmochimica Acta*,
645 *126*, 192-211. https://doi.org/10.1016/j.gca.2013.10.055
646 Gaudin, A., Dehouck, E., & Mangold, N. (2011). Evidence for weathering on early
647 Mars from a comparison with terrestrial weathering profiles. *Icarus*, *216*(1), 257-
648 268. https://doi.org/10.1016/j.icarus.2011.09.004
649 He, H., Ji, S., Tao, Q., Zhu, J., Chen, T., Liang, X., et al. (2017). Transformation of
650 halloysite and kaolinite into beidellite under hydrothermal condition. *American*
651 *Mineralogist*, *102*(5), 997-1005. https://doi.org/10.2138/am-2017-5935
652 Hunt, G. R. (1977). Spectral signatures of particulate minerals in the visible and near

infrared. *Geophysics*, *42*(3), 501-513. https://doi.org/10.1190/1.1440721

Hunt, G. R., & Ashley, R. P. (1979). Spectra of altered rocks in the visible and near infrared. *Economic Geology*, *74*(7), 1613-1629. https://doi.org/10.2113/gsecongeo.74.7.1613

Kawi, S., & Yao, Y. Z. (1999). Saponite catalysts with systematically varied Mg/Ni ratio: Synthesis, characterization, and catalysis. *Microporous & Mesoporous Materials*, *33*(1-3), 49-59. https://doi.org/10.1016/S1387-1811(99)00122-5

Li, S., He, H., Tao, Q., Zhu, J., Tan, W., Ji, S., et al. (2020). Kaolinization of 2:1 type clay minerals with different swelling properties. *American Mineralogist*, *105*(5), 687-696. https://doi.org/10.2138/am-2020-7339

Liu, J., He, H., Michalski, J., Cuadros, J., Yao, Y., Tan, W., et al. (2021a). Reflectance spectroscopy applied to clay mineralogy and alteration intensity of a thick basaltic weathering sequence in Hainan Island, South China. *Applied Clay Science*, *201*, 105923. https://doi.org/10.1016/j.clay.2020.105923

Liu, J., Michalski, J., Tan, W., He, H., & Xiao, L. (2021b). Anoxic chemical weathering under a reducing greenhouse on early Mars. *Nature Astronomy*, *5*, 503–509. https://doi.org/10.1038/s41550-021-01303-5

Lowe, D. R., Bishop, J. L., Loizeau, D., Wray, J. J., & Beyer, R. A. (2020). Deposition of >3.7 Ga clay-rich strata of the Mawrth Vallis Group, Mars, in lacustrine, alluvial, and aeolian environments. *Geological Society of America Bulletin*, *132*(1-2), 17-30. https://doi.org/10.1130/B35185.1

Madejová, J., Janek, M., Komadel, P., Herbert, H. J., & Moog, H. C. (2002). FTIR

675 analyses of water in MX-80 bentonite compacted from high salinary salt solution
676 systems. *Applied Clay Science*, *20*(6), 255-271. https://doi.org/10.1016/S0169-
677 1317(01)00067-9
678 Madejová, J., & Komadel, P. (2001). Baseline studies of the clay minerals society
679 source clays: infrared methods. *Clay and Clay Minerals*, *49*, 410-432.
680 https://doi.org/10.1346/CCMN.2001.0490508
681 Martínez-Alonso, S., Rustad, J. R., & Goetz, A. F. H. (2002). Ab initio quantum
682 mechanical modeling of infrared vibrational frequencies of the OH group in
683 dioctahedral phyllosilicates. Part II: Main physical factors governing the OH
684 vibrations. *American Mineralogist*, *87*(8-9), 1224-1234.
685 https://doi.org/10.2138/am-2002-8-922
686 McKeown, N. K., Bishop, J. L., Noe Dobrea, E. Z., Ehlmann, B. L., Parente, M.,
687 Mustard, J. F., et al. (2009). Characterization of phyllosilicates observed in the
688 central Mawrth Vallis region, Mars, their potential formational processes, and
689 implications for past climate. *Journal of Geophysical Research*, *114*(E2).
690 https://doi.org/10.1029/2008JE003301
691 Michalski, J. R., Bibring, J. P., Poulet, F., Loizeau, D., Mangold, N., Dobrea, E.N., et
692 al. (2010). The Mawrth Vallis Region of Mars: A Potential Landing Site for the
693 Mars Science Laboratory (MSL) Mission. *Astrobiology*, *10*, 687-703.
694 https://doi.org/10.1089/ast.2010.0491
695 Michalski, J. R., Cuadros, J., Bishop, J. L., Darby Dyar, M., Dekov, V., & Fiore, S.
696 (2015). Constraints on the crystal-chemistry of Fe/Mg-rich smectitic clays on

Mars and links to global alteration trends. *Earth and Planetary Science Letters*, *427*, 215-225. https://doi.org/10.1016/j. epsl.2015.06.020

Michalski, J. R., Niles, P. B., Cuadros, J., & Baldridge, A. M. (2013). Multiple working hypotheses for the formation of compositional stratigraphy on Mars: Insights from the Mawrth Vallis region. *Icarus*, *226*, 816-840. https://doi.org/10.1016/j.icarus.2013.05.024

Michalski, J. R., & Noe Dobrea, E. Z. (2007). Evidence for a sedimentary origin of clay minerals in the Mawrth Vallis region, Mars. *Geology*, *35*, 951-954. https://doi.org/10.1130/g23854a.1

Nahon, D., Colin, F., & Tardy, Y. (1982). Formation and distribution of Mg, Fe, Mn-smectites in the first stages of the lateritic weathering of forsterite and tephroite. *Clay Minerals*, *17*(3), 339-348. https://doi.org/10.1180/claymin.1982.017.3.06

Pineau, M., Mathian, M., Baron, F., Rondeau, B., Le Deit, L., Allard, T., & Mangold, N. (2022). Estimating kaolinite crystallinity using near-infrared spectroscopy: Implications for its geology on Earth and Mars. *American Mineralogist*, *107*(8), 1453-1469. https://doi.org/10.2138/am-2022-8025

Prudencio, M. I., Braga, M. A. S., Paquet, H., Waerenborgh, J. C., Pereira, L. C. J., & Gouveia, M. A. (2002). Clay mineral assemblages in weathered basalt profiles from central and southern Portugal: climatic significance. *Catena*, *49*, 77-89. https://doi.org/10.1016/S0341-8162(02)00018-8

Rivera Banuchi, V. B., Liu, W., Yee, N., Legett, C., Glotch, T. D., & Chemtob, S. M. (2022). Ultraviolet photooxidation of Smectite‐bound Fe(II) and implications for

719 the origin of Martian nontronites. *Journal of Geophysical Research: Planets*, *127*,
720 e2021JE007150. https://doi.org/10.1029/2021JE007150
721 Tan, W., Qin, X., Liu, J., Zhou, M., He, H., Yan Wang, C., et al. (2022). Feasibility of
722 visible short-wave infrared reflectance spectroscopy to characterize regolith-
723 hosted rare earth element mineralization. *Economic Geology*, *117*(2), 495-508.
724 https://doi.org/10.5382/econgeo.4877
725 Viviano-Beck, C. E., Seelos, F. P., Murchie, S. L., Kahn, E. G., Seelos, K. D., Taylor,
726 H. W., et al. (2014). Revised CRISM spectral parameters and summary products
727 based on the currently detected mineral diversity on Mars. *Journal of Geophysical*
728 *Research: Planets*, *119*(6), 1403-1431. https://doi.org/10.1002/2014JE004627
729 Viviano, C. E., Moersch, J. E., & McSween, H. Y. (2013). Implications for early
730 hydrothermal environments on Mars through the spectral evidence for carbonation
731 and chloritization reactions in the Nili Fossae region. *Journal of Geophysical*
732 *Research: Planets*, *118*(9), 1858-1872. https://doi.org/10.1002/jgre.20141
733 Wilson, M. J. (2004). Weathering of the primary rock-forming minerals: processes,
734 products and rates. *Clay Minerals*, *39*(3), 233-266.
735 https://doi.org/10.1180/0009855043930133
736 Wray, J. J., Ehlmann, B. L., Squyres, S. W., Mustard, J. F., & Kirk, R. L. (2008).
737 Compositional stratigraphy of clay-bearing layered deposits at Mawrth Vallis,
738 Mars. *Geophysical Research Letters*, *35*(12).
739 https://doi.org/10.1029/2008GL034385
740 Wray, J. J., Murchie, S. L., Squyres, S. W., Seelos, F. P., & Tornabene, L. L. (2009).

741 Diverse aqueous environments on ancient Mars revealed in the southern highlands.
742 *Geology*, *37*(11), 1043-1046. https://doi.org/10.1130/g30331a.1
743 Ye, B., & Michalski, J. R. (2021). Precipitation‐Driven Pedogenic Weathering of
744 Volcaniclastics on Early Mars. *Geophysical Research Letters*, *48*(5), 1–10.
745 https://doi.org/10.1029/2020GL091551
746 Zhang, C., He, H., Tao, Q., Ji, S., Li, S., Ma, L., et al. (2017). Metal occupancy and its
747 influence on thermal stability of synthetic saponites. *Applied Clay Science*, *135*,
748 282-288. https://doi.org/10.1016/j.clay.2016.10.006
749 Zhang, L., Fu, X., Wang, A., & Ling, Z. (2022). Crystallinity effects on the vibrational
750 spectral features of saponite: Implications for characterizing variable crystalline
751 phyllosilicates on Mars. *Icarus* *379*, 114951.
752 https://doi.org/10.1016/j.icarus.2022.114951